Nanoscale Advances

ROYAL SOCIETY OF CHEMISTRY

PAPER

View Article Online
View Journal | View Issue

Cite this: *Nanoscale Adv.*, 2020, **2**, 2859

Metal-enhancement study of dual functional photosensitizers with aggregation-induced emission and singlet oxygen generation†

Mohammad Tavakkoli Yaraki,‡[ab] Fang Hu,‡[b] Soroosh Daqiqeh Rezaei,[ac] Bin Liu *[b] and Yen Nee Tan *[ad]

Photosensitizers with aggregation-induced emission (AIE-PS) are attractive for image-guided photodynamic therapy due to their dual functional role in generating singlet oxygen and producing high fluorescent signal in the aggregated state. However, their brightness and treatment efficiency maybe limited in current practice. Herein we report the first systematic investigation on the metal-enhanced fluorescence (MEF) and singlet oxygen generation (ME-SOG) ability of our newly synthesized AIE-photosensitizers. The Ag@AIE-PS of varied sizes were prepared *via* layer-by-layer assembly with controlled distance between silver nanoparticles (AgNPs) and AIE-PS. A maximum of 6-fold enhancement in fluorescence and 2-fold increment in SOG were observed for the 85nmAg@AIE-PS. Comprehensive characterization and simulation were conducted to unravel the plasmon-enhancement mechanisms of Ag@AIE-PS. Results show that MEF of AIE-PS is determined by the enhanced electric field around AgNPs, while ME-SOG is dictated by the scattering efficiency of the metal core, where bigger AgNPs would result in larger enhancement factor. Furthermore, the optimum distance between AgNPs and AIE-PS to achieve maximum SOG enhancement is shorter than that required for the highest MEF. The correlation of MEF and ME-SOG found in this study is useful for designing new a generation of AIE-photosensitizers with high brightness and treatment efficiency towards practical theranostic application in the future.

Received 4th March 2020
Accepted 9th June 2020

DOI: 10.1039/d0na00182a

rsc.li/nanoscale-advances

1. Introduction

Aggregation-induced emission fluorogens (AIEgens) are a new class of fluorogens that do not emit light in the molecular state, but become highly emissive in the aggregated state due to the restriction of intramolecular motions. Unlike the traditional organic fluorophores, which often suffer from the aggregation-caused quenching (ACQ) effect, AIEgens possess numerous advantages such as good photostability, high brightness, and efficient light-harvesting properties in the aggregated state, which make them especially suitable for biological sensing and imaging applications.[1–4] More recently, AIE-based photosensitizers (AIE-PSs) tailored with both AIE and singlet oxygen generation (SOG) properties have been successfully developed. The use of such AIE-PS for image-guided photodynamic therapy can greatly improve the treatment efficiency by overcoming the intrinsic ACQ effects faced by the traditional photosensitizers with reduced reactive oxygen species (ROS) generation rate in the aggregated state, especially when the loading of PS is high. To synthesize dual-functional AIE-PS, several molecular design strategies such as introducing electron donor (D) and electron acceptor (A) groups,[5,6] tuning the distance between the donor and acceptor,[5] and incorporating auxiliary acceptor groups[5,7] to the AIEgens have been employed to decrease the singlet-triplet energy gap (ΔE_{ST}) and enhance the intersystem crossing (ISC) rate. However, it remains challenging to improve both the SOG efficiency and brightness of fluorescence concurrently by molecular design of AIEgens as both functions consume the excited state.

Plasmonic nanoparticles (NPs) such as gold and silver NPs, have unprecedented ability to localize and enhance their surrounding electric field and confine it into subwavelength volumes due to the excitation of their surface plasmon resonance (SPR) by the incident electromagnetic field, leading to several applications from structural color printing,[8,9] energy storage,[10] and catalysis[11–14] to metal NPs-based biosensors[15–29] development. More recently, these localised SPR effects have been exploited to

[a]*Institute of Materials Research and Engineering, Agency for Science, Technology and Research (A*STAR), 138634, Singapore. E-mail: yennee.tan@ncl.ac.uk*

[b]*Department Chemical and Biomolecular Engineering, National University of Singapore, 4 Engineering Drive 4, Singapore 117585, Singapore. E-mail: cheliub@nus.edu.sg*

[c]*Department of Mechanical Engineering, National University of Singapore, 9 Engineering Drive 1, 117575, Singapore*

[d]*Faculty of Science, Agriculture & Engineering, Newcastle University, Newcastle Upon Tyne NE1 7RU, UK*

† Electronic supplementary information (ESI) available: Details of synthesis procedures and characterization. See DOI: 10.1039/d0na00182a

‡ M. Tavakkoli Yaraki and F. Hu contributed equally to this work.

enhance the optoelectronic properties of functional materials, such as fluorophores and photosensitizers, leading to a new field of studying metal-enhanced fluorescence (MEF)[30–41] and singlet oxygen generation (ME-SOG).[42–48]

To date, several works have been reported to tune the distance between the fluorophore and the metallic surface in controlling the plasmonic-enhancement effects.[49–51] For example, Liang *et al.*[49] employed the layer-by-layer (LBL) technique to control the distance between the conjugated polymeric fluorophore (PFVBT) and silver nanocubes (for up to three bilayers) by using oppositely charged polyelectrolytes for the assembly. In another study, silica-coated silver nanoparticles with varied shell thickness (up to 30 nm) have been used to investigate the interparticle distance-dependent fluorescence of the ultrasmall sized gold nanoclusters.[50] Other than fluorescence, singlet oxygen generation is another interesting property of some fluorophores (also known as photosensitizer, PS), arising from the intersystem crossing in the excited fluorophore. Due to the interactions of the excited fluorophore and plasmonic NPs,[42,48,52–54] photostability and SOG rate of the photosensitizers could be enhanced.[43] For instance, Ke and coworkers[55] have reported the simultaneous enhancement of fluorescence and SOG of the aluminium phthalocyanine on the surface of Au@silica nanorods. However, no correlation was found between the optimum distance for MEF and ME-SOG. To the best of our knowledge, metal-enhancement study of the AIE-based photosensitizer (AIE-PS) and the correlation of their intrinsic fluorescent and singlet oxygen generation properties have not been reported.

In this study, we have conducted a systematic investigation to unravel the correlation of the metal-enhanced fluorescence and metal-enhanced singlet oxygen generation of our newly synthesized dual-functional AIE-PS. Specifically, layer-by-layer technique is utilized to control the distance between the silver nanoparticles (AgNPs) and AIE-PS molecules using differently charged polyelectrolytes. Although the enhancement factors for either fluorescence or singlet oxygen generation is unique for each of the AIE-PSs nanohybrids, it was found that the maximum singlet oxygen occurs at a shorter distance between AgNPs and AIE-PS than that with the maximum fluorescence. The correlation found between the MEF and ME-SOG of Ag@AIE-PS nanohybrids in this study could be useful for designing brightly fluorescent photosensitizers. That will, in turn, open up new opportunities to enhance the unique properties of AIE-based photosensitizers for effective theranostic treatment in the future.

2. Results and discussion

2.1. Synthesis of yellow emissive AIE-PS and study of its photophysical properties

In this study, a new photosensitizer with aggregation-induced emission (**AIE-Y-SOG**) was synthesized as the model AIE-based photosensitizer (AIE-PS) to investigate the enhancement effects by the silver nanoparticles (AgNPs). Fig. 1a shows the synthetic route of **AIE-Y-SOG** formation. Simple heating the mixture of compound **2** with bromoethane in DMF resulted in the formation of yellow emissive **AIE-Y-SOG** in PBS buffer (inset of Fig. 1c). The chemical structure of the purified **AIE-Y-SOG** was confirmed by the nuclear magnetic resonance (NMR) spectroscopy (Fig. S1†). Fig. 1b shows the unique optical properties of the as-synthesized **AIE-Y-SOG**. By introducing an electron-withdrawing group (*i.e.*, vinyl-pyridinium) to tetraphenylethylene (TPE), **AIE-Y-SOG** was obtained with intramolecular charge transfer character. **AIE-Y-SOG** has an absorption maximum at 385 nm with yellow emission at 595 nm.[56] The presence of vinyl-pyridinium moiety renders **AIE-Y-SOG** with positive charges at neutral and acidic pH. Interestingly, the introduction of vinyl-pyridinium also reduces the singlet-triplet gap (ΔE_{ST}) of the **AIE-Y-SOG**,[6] endowing it with the unique photosensitizing ability, which can be utilized for photodynamic therapy (PDT).[57–59] The large Stokes shift (about 210 nm) in **AIE-Y-SOG** could be attributed to the strong intramolecular charge transfer as a result of the incorporation of the electron-donating and accepting groups to the TPE moiety.[56]

The AIE behavior of **AIE-Y-SOG** was investigated in a mixture of dimethyl siloxane (DMSO) as good solvent and PBS as a poor solvent. As shown in Fig. 1c, the **AIE-Y-SOG** shows red emission (cantered at 680 nm, inset of Fig. 1c) in the DMSO solution. The emission intensity was decreased gradually as the PBS fraction was increased up to 80%, due to the twisted intramolecular charge transfer (TICT) effect.[60,61] Then, the fluorescence intensity was recovered with blue-shifted emission peaked at 595 nm, showing yellow emission in PBS buffer (inset of Fig. 1c). This enhanced fluorescence effects (as compared with the diluted **AIE-Y-SOG** in DMSO) could be attributed to the restriction of intramolecular motions, which is activated by the formation of **AIE-Y-SOG** nanoparticles (NPs) in PBS solution. Fig. S2† shows that **AIE-Y-SOG** NPs in PBS have an average hydrodynamic diameter of 155 ± 4 nm as measured by dynamic light scattering (DLS). The fluorescence quantum yield of **AIE-Y-SOG** NPs was calculated to be 4.9%, measured against the 4-(dicyanomethylene)-2-methyl-6-(*p*-dimethylaminostyryl)-4H-pyran (DCM) as reference.

2.2. Investigation of the metal-enhanced fluorescence of AIE-PS

2.2.1 Formation of Ag@AIE-Y-SOG nanohybrids through layer-by-layer assembly. To study the plasmonic enhancement effect of **AIE-Y-SOG**, we have synthesized different sizes of AgNPs using tannic acid as the stabilizer as shown in Fig. S3a.† The size distributions of AgNPs with an average diameter of 25 nm, 40 nm, and 85 nm, were determined by the dynamic light scattering (Fig. S3b†) and transmission electron microscopy (Fig. S4†) measurement. All of the as-synthesized AgNP are negatively charged as shown by the zeta potential measurement (Fig. 2a), indicating the presence of tannic acid as capping agent, which is consistent with the literature.[62]

Upon successful synthesis of the well-dispersed AgNPs, a suitable pair of oppositely charged polyelectrolytes (PEs) were selected to enable the layer-by-layer (LBL) assembly onto the AgNPs surface. Based on the consideration of molecular weight and structure of PEs, polyethyleneimine (PEI, $M_w = 2000$) and

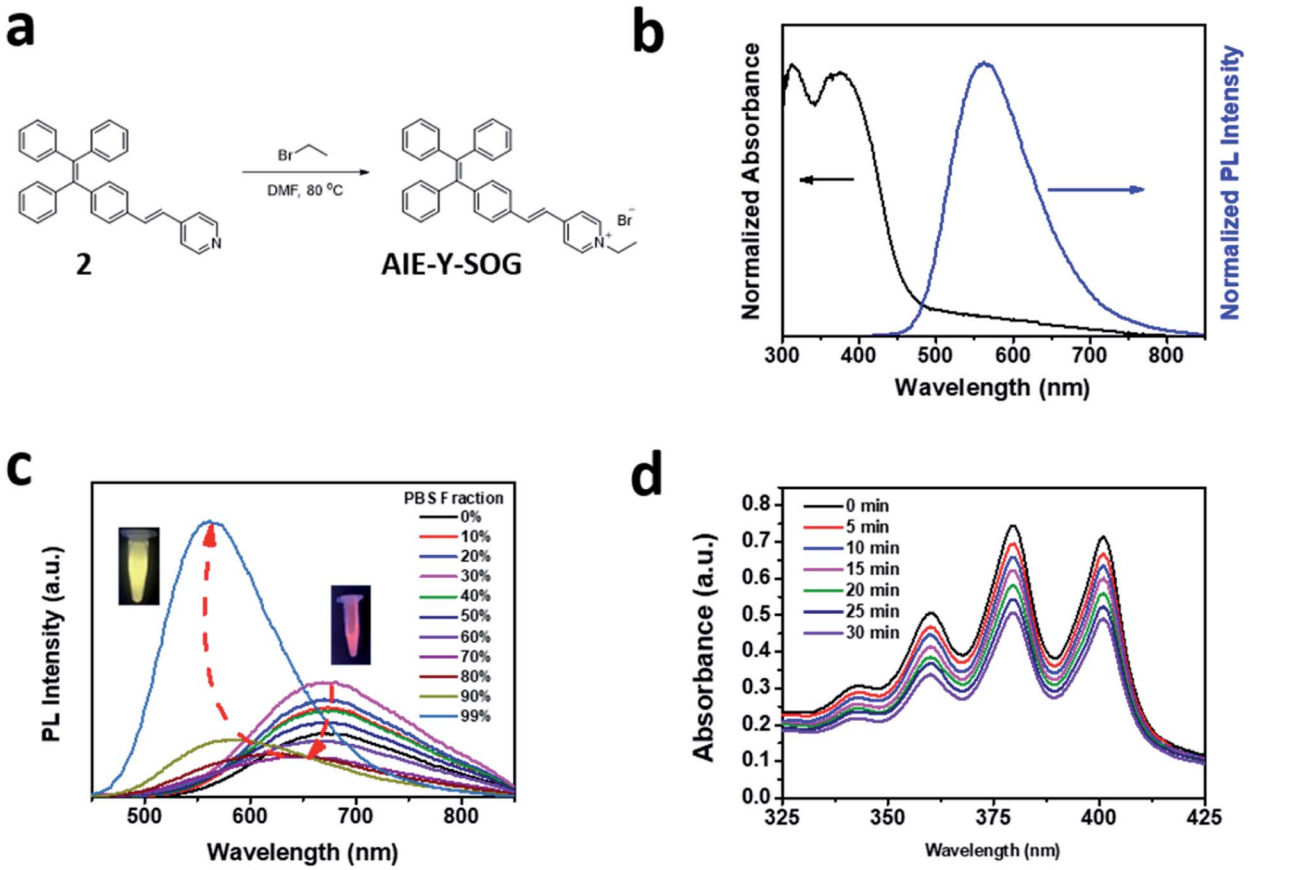

Fig. 1 (a) Synthetic route of **AIE-Y-SOG**. (b) Normalized absorbance (black line) and normalized fluorescence (blue line) spectra of **AIE-Y-SOG** in PBS buffer, $\lambda_{ex} = 385$ nm. (c) Effect of solubility of **AIE-Y-SOG** in PBS/DMSO mixture at different fraction on photoluminescence (PL) spectra. Inset of 1c shows the color photograph of the **AIE-Y-SOG** in DMSO (right) and PBS (left) solution, respectively under 365 nm UV excitation. (d) Degradation of 9,10-anthracenediyl-bis(methylene)dimalonic acid (ABDA, 50 μM) in the presence of **AIE-Y-SOG** (10 μM) in PBS buffer under white light (40 mW cm^{-2}) irradiation at different duration.

poly(styrene sulfuric acid) sodium salt (PSS, $M_w = 70\,000$) were selected in this study (Fig. 2a) to form the bilayers of suitable thickness in controlling the distance between AgNPs and AIEgens for the metal-enhancement study. To obtain a thin bilayer of PEs, suitable solution pH (*i.e.*, pH = 3) in consideration of the pK_a and pK_b of the two polyelectrolytes and NaCl concentration (10 mM)[63–65] were selected for the LBL assembly of PEI and PSS onto AgNPs. The presence of tannic acid on the surface of AgNPs enables the adsorption of positively charged PEI on the negatively charged AgNPs. Fig. 2b shows the variation of the zeta potential for the 25 nm AgNPs after deposition of each layer of polyelectrolyte, indicating the successful assembly of PEI or PSS in each step. As shown in Fig. 2c–e, the as-formed PEs-coated AgNPs are stable throughout the LBL assembly process since no apparent redshift in the SPR peak or change in the intensity of extinction at the higher wavelengths (>600 nm) were observed. Based on the TEM images of PEs-coated AgNPs (see insets of Fig. 2c for 25Ag/1BL and Fig. 2e for 85Ag/1BL, respectively), the thickness of each PEI/PSS bilayer is estimated to be around 3.5 nm.

2.2.2 Distance and size-dependent fluorescence enhancement of Ag@AIE-PS. Firstly, distance-dependent study of the Ag@AIE-PS nanohybrids for fluorescence enhancement was conducted by controlling the spaces between AgNPs and **AIE-Y-SOG** (10 μM) through the LBL assembled PEI/PSS bilayers. Due to the aggregation-induced emission nature of the **AIE-Y-SOG**, the MEF effects of Ag@**AIE-Y-SOG** was compared with the same amount of **AIE-Y-SOG** adsorbed on silica nanoparticles (SiNP). The fluorescent of **AIE-Y-SOG** was turned on when they were adsorbed/aggregated on the surface of either AgNPs or SiNP in water solution. The fluorescence enhancement factor is defined by the ratio of the maximum photoluminescent (PL) intensity of Ag@**AIE-Y-SOG** to the Si@**AIE-Y-SOG** in the control sample. Based on the PL intensity of the Ag@**AIE-Y-SOG**, the fluorescence enhancement factor (EF_{MEF}) was calculated:

$$\text{Fluorescence enhancement factor } (EF_{MEF}) = \frac{\text{Max\_PL}_{Ag@AIE}}{\text{Max\_PL}_{Si@AIE}} \quad (1)$$

As can be seen in Fig. 3a, the fluorescence of **AIE-Y-SOG** was quenched at the close vicinity of AgNPs when no polyelectrolyte (0BL sample) was introduced. This phenomenon is due to the significant energy transfer rate from the excited **AIE-Y-SOG** to

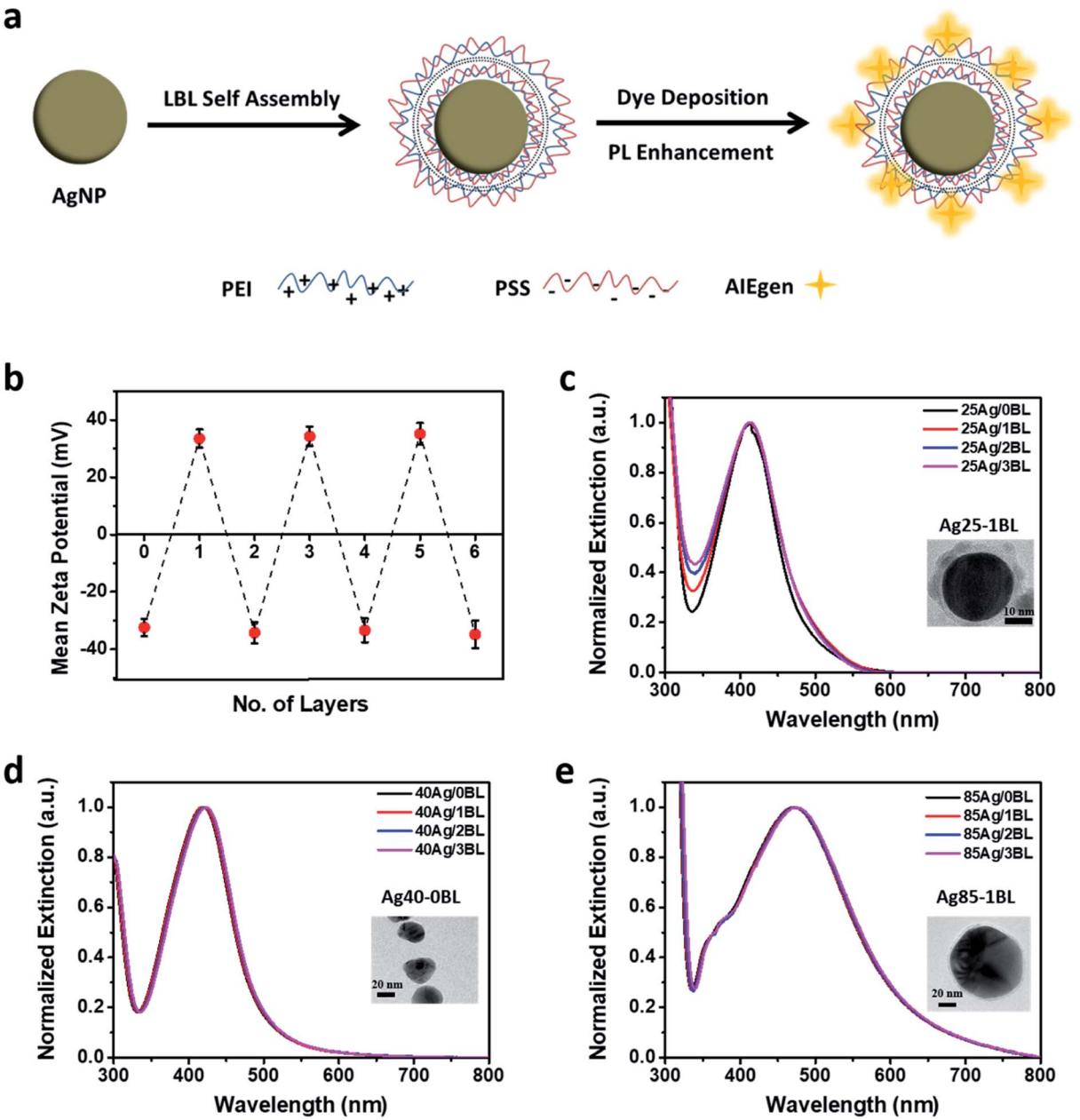

Fig. 2 (a) Schematic diagram showing the layer-by-layer assembly of oppositely charged polyelectrolytes composed of polyethyleneimine (PEI) and poly(styrene sulfuric acid) sodium salt (PSS) to control the distance between AIEgen and AgNP, (b) zeta potential of PEs-coated AgNPs as a function of polyelectrolytes bilayers (odd layer numbers for PEI and even layer numbers for PSS), (c) normalized extinction of 25 nm AgNPs with different PEI/PSS bilayers. Inset shows the TEM image of the 25 nm AgNPs with 1 bilayer (*i.e.*, 25Ag/1BL), (d) normalized extinction of 40 nm AgNPs with different PEI/PSS bilayers. Inset shows the TEM image of 40 nm AgNPs without bilayers (*i.e.*, 40Ag/0BL), (e) normalized extinction of 85 nm AgNPs with different PEI/PSS bilayers. Inset shows the TEM image of 85 nm AgNPs with 1 bilayer (*i.e.*, 85Ag/1BL).

the AgNPs surface. It was found that the fluorescence enhancement factor increases with the increasing number of bilayers and reaches a maximum before decreasing with the increased distance. This trend indicates the distance-dependent nature of the MEF of Ag@**AIE-Y-SOG** in the nanohybrid system. The maximum MEF (~1.4-fold enhancement) was obtained for the nanohybrids consisting of 25 nm AgNPs with 2 PEI/PSS bilayers, which is estimated to have a spacing of 7 nm between the AgNPs and **AIE-Y-SOG**.

To investigate the size-dependent MEF of **AIE-Y-SOG**, two other sizes of AgNPs (*i.e.*, 40 nm and 85 nm) were synthesized. Similar LBL assembly conditions were used to form the Ag@**AIE-Y-SOG** nanohybrids with different number of PEI/PSS bilayers (BL). Fig. 3b shows the distance-dependent MEF effect for different sizes of AgNPs, where 2BL is the optimum distance for all the sizes of AgNPs tested in this study. It was also found that the fluorescence enhancement factor (EF_{MEF}) increases with the increasing sizes of AgNPs. The highest

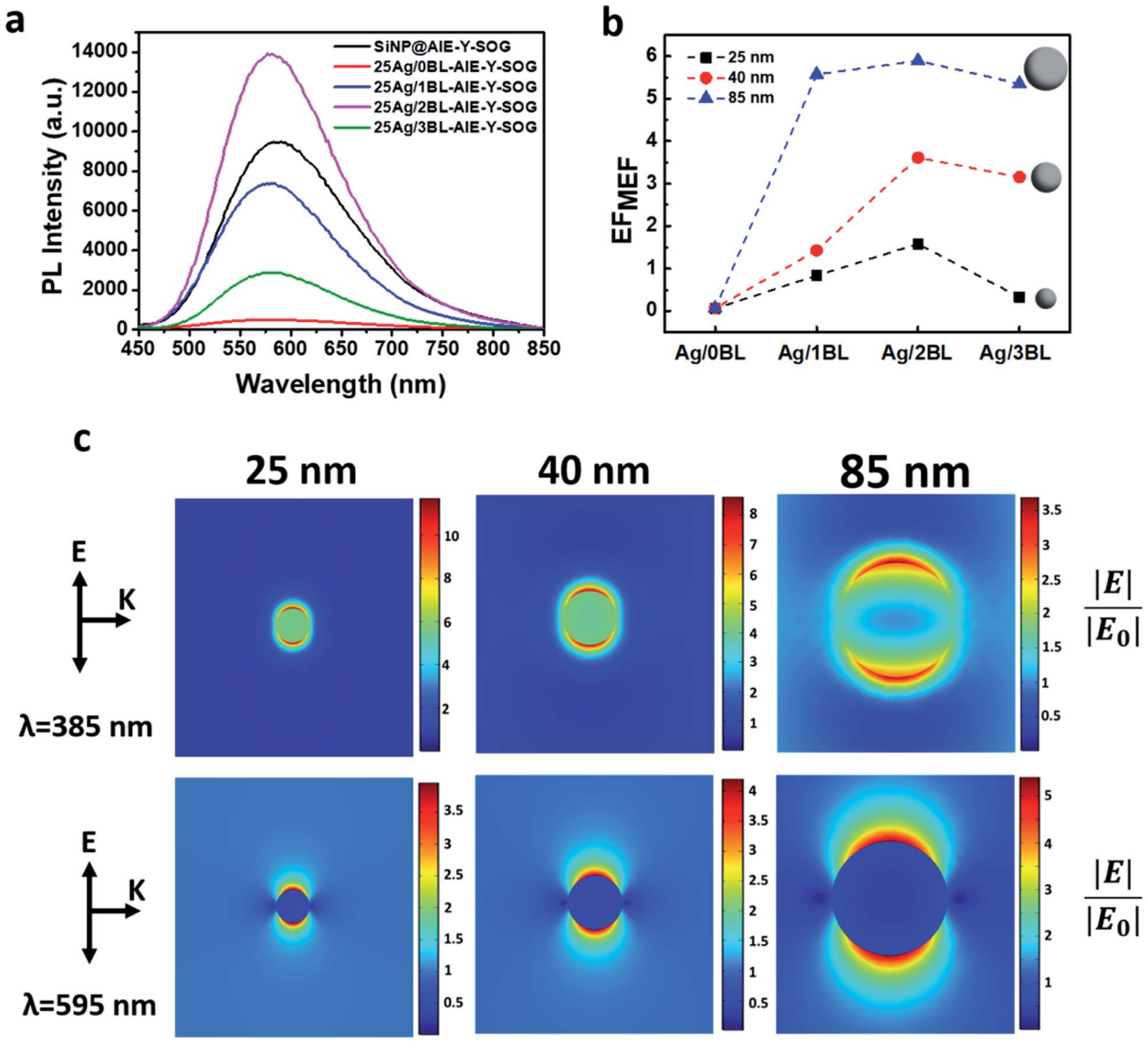

Fig. 3 (a) Distance-dependent MEF of 25 nm Ag@**AIE-Y-SOG**, (b) size-dependent and distance-dependent fluorescence enhancement factor for **AIE-Y-SOG**, (c) simulated enhanced electric field ($|E|/|E_0|$) distribution around AgNPs of different sizes (25, 40, and 85 nm) excited at 385 nm (top row) and 595 nm (bottom row). The arrows for *E* and *K* indicate the direction of electric field polarization and incident light propagation, respectively.

enhancement of 6-fold was achieved for the 85 nm Ag@**AIE-Y-SOG** sample with 2 bilayers. Simulation has been conducted to better understand the plasmon-enhanced fluorescence. The enhanced electric field ($|E|/|E_0|$) around the AgNPs of different sizes excited at the 385 nm wavelength (*i.e.*, excitation wavelength of **AIE-Y-SOG**) are shown in Fig. 3c (top row). Although the enhanced electric field on the surface of 25 nm AgNPs is stronger than the 40 nm and 85 nm AgNPs, the quenching effect of a small AgNPs (*e.g.*, 25 nm) is much higher than the large NPs (*e.g.*,85 nm) as reported in other literature.[66,67] Hence, the EF_{MEF} is higher when the fluorophore locates around a bigger AgNP. Another possible reason is the volumetric effect of the enhanced electric field around AgNPs, where bigger nanoparticles can enhance the electric field in a more prominent space/distance from the surface of metal NPs. Hence, more fluorophore molecules could be located there and subsequently be excited.[68,69] To assess this volumetric effect, the surface average enhanced electric field around the AgNPs at different distances was calculated. As can be seen in Fig. S5,† the electric field at the surface of 25 nm AgNP is higher than the 40 nm and 85 nm AgNPs. The magnitude of the electric field is however, in a reverse order of AgNP (85 nm) > AgNP (40 nm) > AgNP (25 nm) for more than 6 nm from the surface of AgNP. These results are in good agreement with the experimental data presented in Fig. 3b where the MEF effect is highest for the **AIE-Y-SOG** on 85Ag/2BL as compared with the AgNPs of the smaller particle size and same number of bilayers. In addition, the enhanced electric field around the AgNPs at the 595 nm wavelength (*i.e.*, emission wavelength of **AIE-Y-SOG**) was simulated (Fig. 3c, bottom row). The enhanced electric field at this wavelength

shows that the electrons in AgNPs could be excited when **AIE-Y-SOG** is emitting fluorescence, leading to the plasmonic-coupling effect of AgNPs in MEF. Furthermore, it was found that the magnitude of the enhanced electric field is in order of AgNP (85 nm) > AgNP (40 nm) > AgNP (25 nm), which is aligned with the size-dependent fluorescence enhancement factor for **AIE-Y-SOG** as observed experimentally in Fig. 3b.

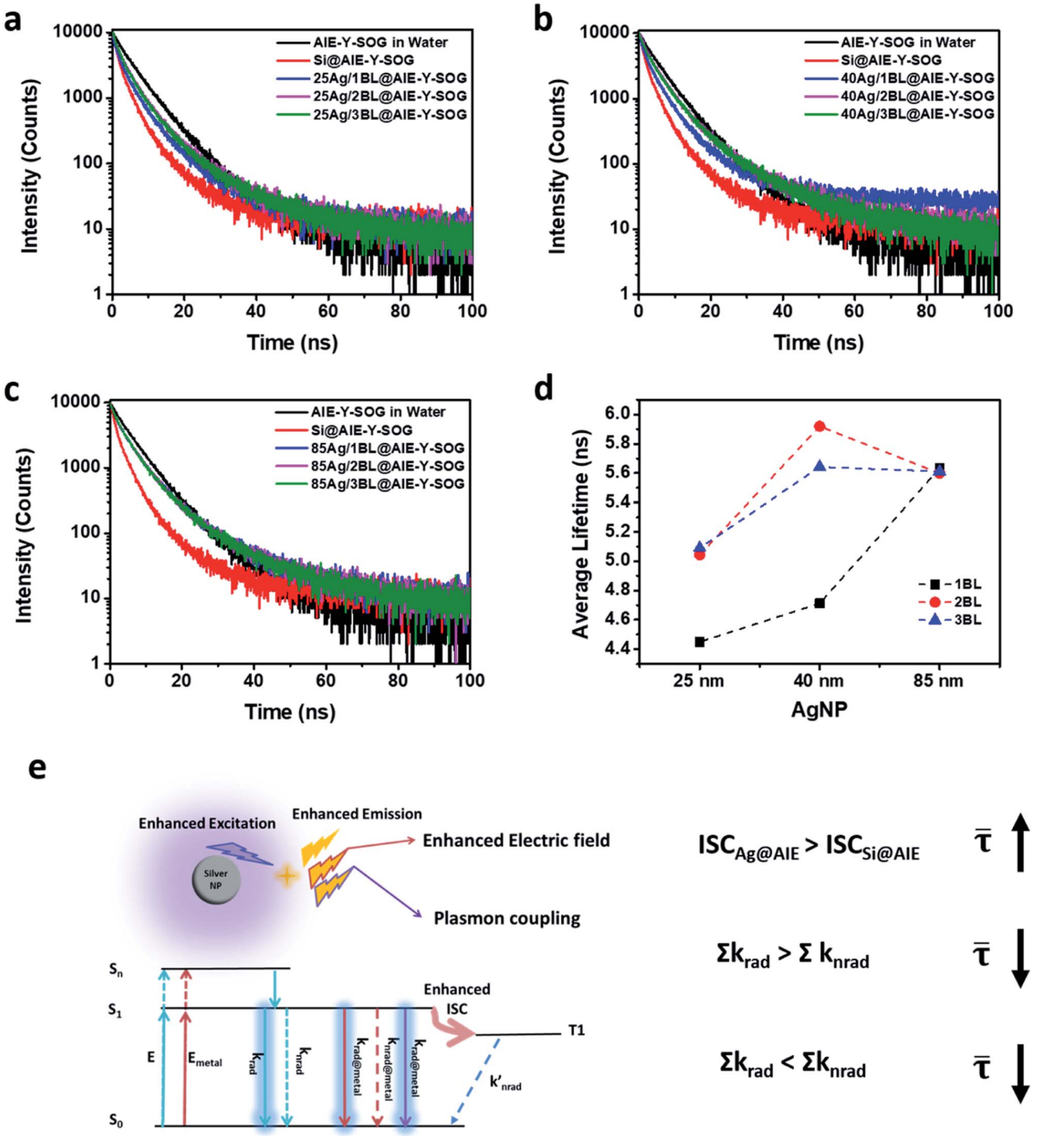

Fig. 4 Fluorescence decay profile of Ag@**AIE-Y-SOG** with different PEI/PSS bilayers and AgNPs sizes (a) 25 nm AgNPs, (b) 40 nm AgNPs, and (c) 85 nm AgNPs. (d) Average fluorescence lifetime ($\bar{\tau}$) for Ag@**AIE-Y-SOG** samples with 1 (square), 2 (sphere), and 3 (triangle) PEI/PSS bilayers. (e) Simplified Jablonski diagram for a typical AIE-PS in the vicinity of AgNPs. Σk_{rad} is the summation of intrinsic radiative decay rate in AIE-PS (k_{rad}) and radiative decay rate due to the presence of metal NPs ($k_{rad@metal}$). Σk_{nrad} is the summation of intrinsic non-radiative decay rate in AIE-PS (k_{nrad}) and non-radiative decay rate due to the presence of metal NPs ($k_{nrad@metal}$). The average fluorescence lifetime is defined as $\bar{\tau} = 1/(\Sigma k_{rad} + \Sigma k_{nrad})$ for a classical fluorophore.

2.2.3 Fluorescent lifetime measurement and mechanism study of Ag@AIE-PS. To further investigate the MEF mechanism of this newly synthesized **AIE-Y-SOG** photosensitizer with different sizes of AgNPs (*i.e.*, 25, 40 and 85 nm), fluorescence lifetime measurement was conducted and fitted using a bi-exponential decay model as shown in Fig. 4. Table S1† summarizes the fluorescence lifetime data for different Ag@**AIE-Y-SOG** samples with varied number of bilayers (or distance). Fig. 4a shows that the **AIE-Y-SOG** has a shorter lifetime on silica nanoparticles than that in the water medium, which could presumably be due to the aggregation of **AIE-Y-SOG** molecules on the surface of silica nanoparticles. The same trend has also been observed for the previously reported PFVBT conjugated polymer system when it is in the molecular state (in water) and aggregated state (loaded on silica NPs).[49] In addition, the fluorescence lifetime of all samples containing AgNPs increases as compared to the control sample loaded on SiNP (*i.e.*, from 3.64 ns for Si@**AIE-Y-SOG** to >4 ns for all Ag@**AIE-Y-SOG** samples). Based on the theory of MEF for a classical fluorophore, the fluorescence lifetime should remain constant (*i.e.*, due to plasmonic coupling effect) or decrease (*i.e.*, due to enhanced electric field around the metal nanoparticle) when a fluorophore locates in the vicinity (~<20 nm) of metal NPs.[70,71] As **AIE-Y-SOG** itself is also a photosensitizer, the excited electrons may undergo intersystem crossing process, which could be changed due to the enhanced electric field around AgNPs,[52,72] leading to the increase in its fluorescence lifetime. Hence, the longer fluorescence lifetime as observed for all the Ag@**AIE-Y-SOG** samples tested in this study (Table S1†) could be due to the balancing changes among the radiative decays, non-radiative decays and intersystem crossing rate as a result of the enhanced electric field around AgNPs and plasmonic coupling effect. Fig. 4d shows the size effect of AgNPs on the average lifetime of Ag@**AIE-Y-SOG** when it is located at different distances from the surface of AgNPs. The Jablonski diagram for a typical AIE-PS in the vicinity of AgNP and the effect of changes in the ISC rate, radiative decay rates (Σk_{rad}) and non-radiative decay rates (Σk_{nrad}) on the average fluorescence lifetime is summarized in Fig. 4e. This can be used to explain the observed fluorescence lifetime of the 25 nm Ag@**AIE-Y-SOG** samples prepared at different number of bilayer (BL) (*i.e.*, 4.45 ns, 5.04 ns and 5.09 ns for 1BL, 2BL and 3BL separation thickness, respectively) which is shorter than that for the 85 nm Ag@**AIE-Y-SOG** samples (*i.e.*, 5.63 ns, 5.60 ns and 5.61 ns for 1BL, 2BL and 3BL separation thickness, respectively), due presumably to the relatively larger energy transfer from the excited AIE-PS molecules to the smaller AgNPs ($\Sigma k_{rad} < \Sigma k_{nrad}$).[66,67] Distance-dependent effect was also observed for the fluorescence lifetime of Ag@**AIE-Y-SOG** samples with the same AgNPs size. That is, the fluorescence lifetimes for 1BL samples are shorter than the 2BL and 3BL samples, respectively. This could be attributed to the large non-radiative decay rates for the AIE-PS around the small AgNPs or near the metallic surface ($\Sigma k_{rad} < \Sigma k_{nrad}$).[73] However, when the non-radiative decay rates are not dominant in a further distance (*e.g.* 2BL and 3BL), the fluorescence lifetime of Ag@**AIE-Y-SOG** samples with the same bilayer is found to be 5.92 ns for the 40Ag/2BL@**AIE-Y-SOG** and 5.59 ns for the 85Ag/2BL@**AIE-Y-SOG**. This trend could be described by the MEF effect where the radiative decay rates for 85 nm Ag@**AIE-Y-SOG** samples is much larger than that for the 40 nm Ag@**AIE-Y-SOG** samples ($\Sigma k_{rad} > \Sigma k_{nrad}$), causing a slight decrease in the fluorescence lifetime.

To better understand the MEF effects of the AIE-based photosensitizer, two other AIEgens were synthesized (see ESI, Page S2†). They are the blue emissive AIE-B without SOG ability (inset of Fig. 5a) and the red emissive AIE-R-SOG with SOG ability (inset of Fig. 5c). AIE-B is composed of an iconic AIE core, TPE[74] and positively charged ammonium salt, which is linked by alkoxy. Similar to TPE,[75] it has an ultraviolet-visible absorption, with a maximum absorbance peak at 321 nm, exhibiting blue emission at 485 nm. The AIE-B can neither generate singlet oxygen nor form AIE nanoparticles in PBS solution (Scheme S1, Fig. S6, and S7†). On the other hand, AIE-R-SOG is an improved AIE-PS from the **AIE-Y-SOG** by decorating two electron-donating methoxy groups. The donor–acceptor effect makes the absorption and emission of AIE-R-SOG further red-shifted to 405 nm and 625 nm, respectively. Meanwhile, the AIE-R-SOG also possesses the photosensitizing ability to generate singlet oxygen (Fig. S8†). It can also form the AIE nanoparticles in PBS solution with a twisted intramolecular charge transfer behavior, as reported previously.[61]

The Ag@AIE-B and Ag@AIE-R-SOG nanohybrids were then prepared using the same pairs of PEI/PSS polyelectrolytes and assembly conditions. Their MEF effects were studied and compared with the Ag@**AIE-Y-SOG** (Fig. 5). As can be seen in Fig. 5a and c, the maximum PL intensity for both AIE-B and AIE-R-SOG was observed at a distance of three bilayers. According to Table S2† (and Fig. 5b), the Ag@AIE-B samples has a longer fluorescence lifetime as compared to the control sample of AIE-B loaded on silica NPs. This result suggested that the fluorescence dynamic of AIE-B depended on its distance from the surface of AgNPs. Since AIE-B can neither generate singlet oxygen nor form AIE nanoparticles in PBS solution, its fluorescence behaviour should follow the classical model, *i.e.*, fluorescence lifetime is a function of the radiative decay rate and non-radiative decay rate. These two decay rates are manipulated when the AIE-B is placed in the vicinity of AgNPs, resulting in changes in the fluorescence lifetime for the samples prepared with varied separation distances between the AIE-B and AgNPs. Although no change or a decrease in fluorescence lifetime is expected in MEF system, there are a few reports on the increase in the fluorescence lifetime of the fluorophore in the vicinity of metallic NPs.[76] In addition, the lower fluorescence enhancement of AIE-B could be attributed to the smaller overlap between the absorbance of the AIE-B (centred at 321 nm) and the extinction spectra of AgNPs.[77,78] Likewise, the fluorescence lifetime of Ag@AIE-R-SOG samples are slightly longer than the control sample loaded on silica NPs (Fig. 5d and Table S3†). This is because AIE-R-SOG is a photosensitizer molecule, which changes in the radiative decay rates, non-radiative decay rates and intersystem crossing rate determine the fluorescence lifetime of AIE-R-SOG when placing near to the AgNPs. The same phenomenon was observed in the Ag@**AIE-Y-SOG**

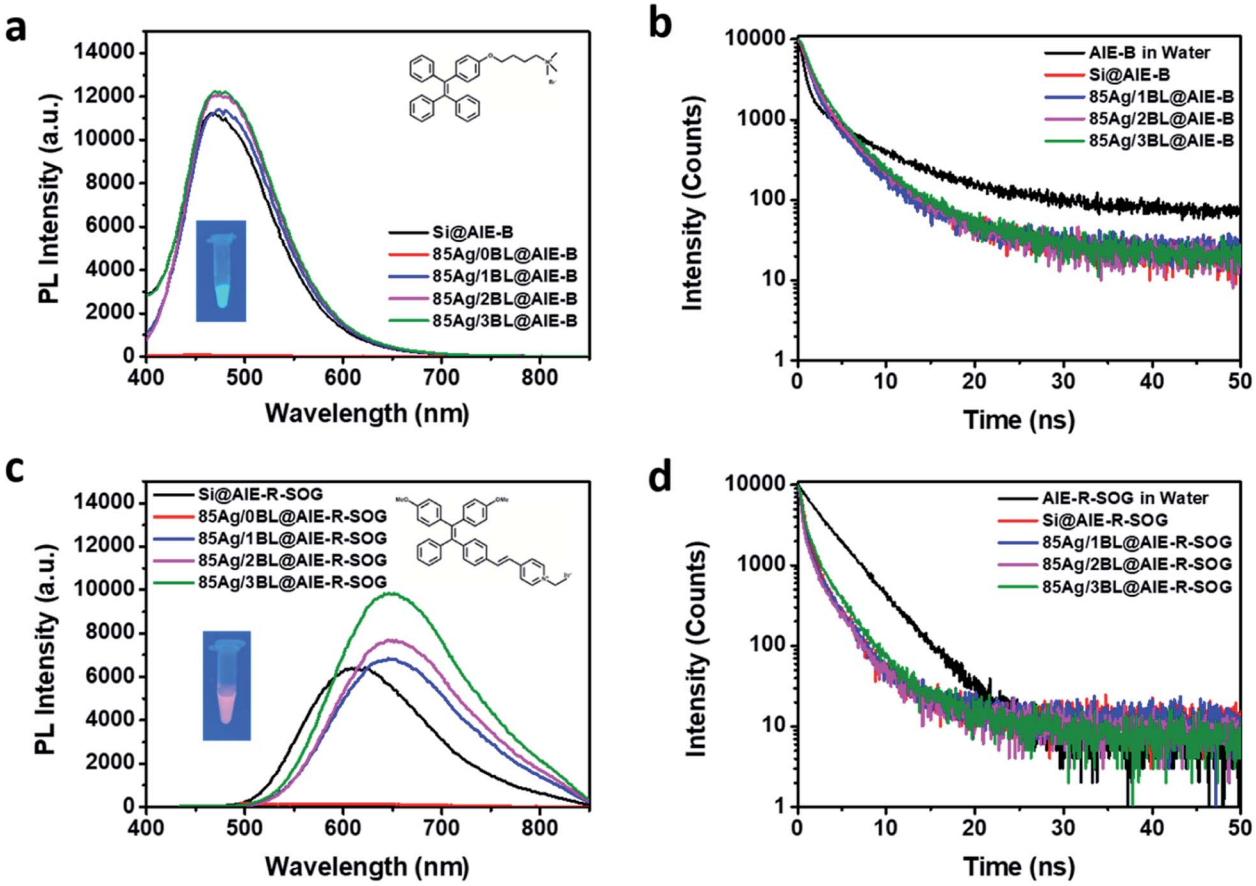

Fig. 5 Distance-dependent MEF (left) and fluorescence decay profile (right) of (a and b) 85 nm Ag@AIE-B and (c and d) 85 nm Ag@AIE-R-SOG with different bilayers of PEI/PSS, in water, and their control samples loaded on SiNP and in PBS, respectively. The insets of (a and b) show the chemical structure (top right) and fluorescence color (bottom left) of each AIEgen in the aggregated state under 365 nm UV light.

nanohybrids with AgNPs of different sizes and number of PEI/PSS bilayers.

2.3. Investigation of the correlation between MEF and ME-SOG of AIE-PS

To understand the correlation between the metal-enhanced fluorescence (MEF) and metal-enhanced singlet oxygen generation (ME-SOG) of AIE-PSs, the SOG rate of different AIE-PSs (*i.e.*, **AIE-Y-SOG** and AIE-R-SOG) in the presence of AgNPs core was measured using 9,10-anthracenediyl-bis(methylene) dimalonic acid (ABDA) as an indicator. ABDA is an anthracene derivative, which can trap the singlet oxygen molecule and convert to an endoperoxide product. The disappearance of the characteristic absorption peak of ABDA indicates the amount of consumed ABDA and correspondingly, the amount of produced singlet oxygen by the photosensitizer. Thus, the degradation of ABDA was monitored by its UV-vis spectra (Fig. S9†). Similar to MEF, the enhanced electric field around the silver nanoparticles results in the enhanced excitation rate, which in turn increases the population of electrons in the excited singlet state (S_1). The excited electrons in the singlet state may go through the intersystem crossing process ($S_1 \rightarrow T_1$) and produce excited electrons in the triplet state (T_1). Finally, the increased population of electrons in T_1 will result in a higher amount of singlet oxygen generation (see Fig. 4e).[52,72] Fig. S10a† shows the ME-SOG effect of Ag@**AIE-Y-SOG** prepared using different size of AgNPs and numbers of bilayers similar to the MEF study. It was found that the singlet oxygen generation has an opposite trend as compared with the MEF of Ag@**AIE-Y-SOG** (Fig. 3b). The ME-SOG effect is maximum when AgNPs directly contacted with the **AIE-Y-SOG** (*i.e.*, 0BL) and the observed enhancement effects decreased with increasing distance (number of bilayers) between them. The enhancement factor of singlet oxygen generation (EF_{SOG}, see Page S4 in ESI† for detailed calculation) is a function of the AgNPs size (Fig. S10a†). The calculated EF_{SOG} for the 85 nm Ag@**AIE-Y-SOG** is higher than the 25 nm Ag@**AIE-Y-SOG**. The simulated scattering efficiencies of AgNP samples indicate that 85 nm AgNP has a higher scattering efficiency when they exposed to the white light (Fig. S10b†). The correlation between ME-SOG and scattering efficiency in our study is in agreement with the literature,[54,79] indicating the important role of the metal NP's scattering efficiency in enhancing singlet oxygen generation. The slight increase in EF_{SOG} for the 2BL Ag@**AIE-Y-SOG** samples could be attributed to an increase in the intersystem crossing and the competition between different pathways for excited electrons. Planas *et al.*[42] have reported the

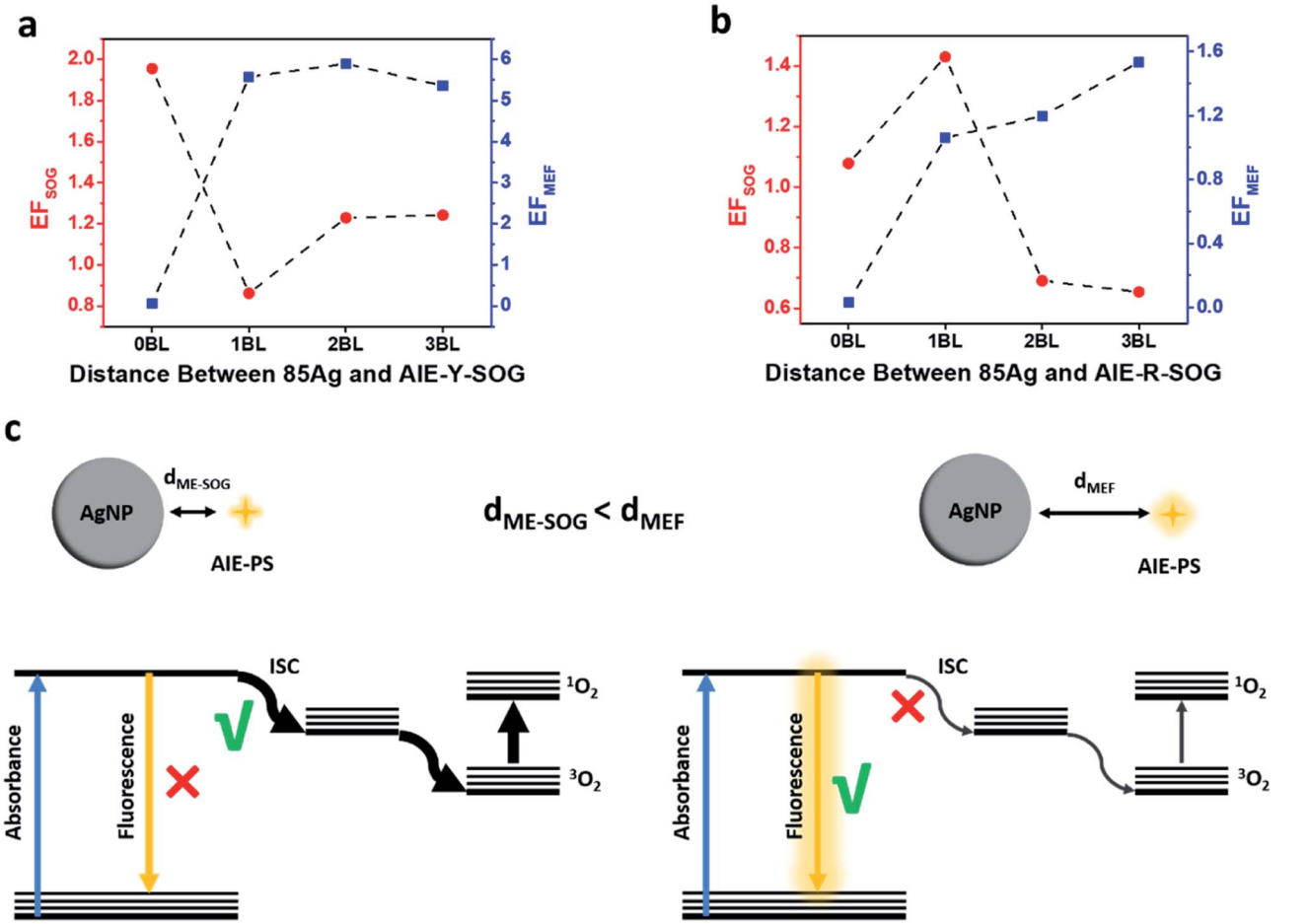

Fig. 6 Correlation between ME-SOG (red sphere) and MEF (blue square) for (a) **AIE-Y-SOG** and (b) AIE-R-SOG using 85 nm AgNP with different PEI/PSS bilayers. (c) Simplified Jablonski diagrams showing the MEF (right scheme) and ME-SOG (left scheme) mechanism of the AIE-PS nanohybrids occur at different optimum AgNPs to AIE-PS distance for maximum plasmonic enhancement.

distance-dependent ME-SOG effects of the AgNPs@Rose Bengal nanohybrid where the maximum enhancement occurs at a distance of 20 nm between the 67 nm AgNPs and Rose Bengal as the photosensitizer. However, our results for the **AIE-Y-SOG** show a different trend where the maximum ME-SOG occurs at the surface of AgNPs (*i.e.*, 0 bilayer), which is in agreement with the results reported by Zhang *et al.*[52] We further studied the ME-SOG of AIE-R-SOG with 85 nm AgNPs at distance controlled by the similar number of bilayers as the 85 nm Ag@**AIE-Y-SOG** (Fig. S11†). Comparing the distance-dependent MEF and ME-SOG data for the two studied AIE-PSs (*i.e.*, **AIE-Y-SOG** and AIE-R-SOG in Fig. 6a and b) reveals that the optimum distance of ME-SOG ($d_{\text{ME-SOG}}$) required to achieve the maximum enhancement factor is shorter than that required for the maximum fluorescence intensity (d_{MEF}) in the Ag@AIE-PS nanohybrid system. In addition, these optimum distances (*i.e.*, $d_{\text{ME-SOG}}$ and d_{MEF}) are unique for each Ag@AIE-PS nanohybrid system and should be obtained experimentally. According to the classical Jablonski diagrams as shown in Fig. 6c, either the intersystem crossing (ISC) rate or radiative decay rates could be enhanced in AIE-PS placed in a proximity of the silver nanoparticle. Since the ISC is a non-radiative process, it tends to be enhanced at a shorter distance (*e.g.*, 1 bilayer thickness for the Ag@AIE-R-SOG with an estimated $d_{\text{ME-SOG}} = 3.5$ nm), where the non-radiative decay rates are enhanced dramatically as compared to the radiative decay rates. In contrast, radiative decay rates become dominant at a longer distance (*e.g.*, 3 bilayer thickness for the Ag@AIE-R-SOG with estimated $d_{\text{MEF}} = 10.5$ nm). The correlation as observed in study is important in designing the effective metal-enhanced AIE-based photosensitizer for effect theranostic treatment.

3. Conclusion

In summary, we have systematically studied the metal-enhanced fluorescence (MEF) and singlet oxygen generation (ME-SOG) of the Ag@AIE-PS nanohybrids prepared *via* layer-by-layer assembly of PEI/PSS polyelectrolytes to control the distance between AgNPs and AIE-PS. Both sizes and distance-dependent effects of Ag@AIE-PS on the MEF and ME-SOG were carefully investigated. It was found that the 85 nm Ag NPs could lead to about 6-fold enhancement in fluorescence and 1.95-fold increment in singlet oxygen generation for the yellow emissive **AIE-Y-SOG** synthesized in this study. While the

enhancement of singlet oxygen generation was mainly determined by the enhanced excitation due to a stronger scattering around the bigger AgNPs, the fluorescence enhancement of AIE-PS was determined by two competing processes, *i.e.*, (1) enhanced excitation and plasmonic-coupling due to enhanced electric field around the AgNPs and (2) energy transfer to the metallic NPs. Time-resolved fluorescence study also indicates that the balance among radiative decay rate, non-radiative decay rate, and intersystem crossing rate in AIE-PSs could be changed in the vicinity of AgNPs. Nonetheless, the optimum distance of ME-SOG required to achieve the maximum enhancement factor (*e.g.*, 0BL for **AIE-Y-SOG**) is usually shorter than that required for the highest MEF (*e.g.*, 2BL for **AIE-Y-SOG**). This information is useful for the development of effective AIE-PS based theranostic agents with high brightness and improved efficacy for practical application of image-guided PDT treatment in the future.

Conflicts of interest

There are no conflicts to declare.

Acknowledgements

M. T. Y. would like to thank Dr Aarash Nemati for the discussion on simulations. M. T. Y. and S. D. R. acknowledge the scholarship provided by the Agency for Science, Technology and Research (A*STAR) through the Singapore International Graduate Award (SINGA). The authors also acknowledge the support from the Institute of Materials Research and Engineering, National University of Singapore and Newcastle University for the collaborative research.

References

1 J. Liang, B. Z. Tang and B. Liu, *Chem. Soc. Rev.*, 2015, **44**, 2798–2811.
2 D. Ding, K. Li, B. Liu and B. Z. Tang, *Acc. Chem. Res.*, 2013, **46**, 2441–2453.
3 Z. Song, W. Zhang, M. Jiang, H. H. Sung, R. T. Kwok, H. Nie, I. D. Williams, B. Liu and B. Z. Tang, *Adv. Funct. Mater.*, 2016, **26**, 824–832.
4 J. Geng, W. L. Goh, C. Zhang, D. P. Lane, B. Liu, F. Ghadessy and Y. N. Tan, *J. Mater. Chem. B*, 2015, **3**, 5933–5937.
5 S. Xu, W. Wu, X. Cai, C.-J. Zhang, Y. Yuan, J. Liang, G. Feng, P. Manghnani and B. Liu, *Chem. Commun.*, 2017, **53**, 8727–8730.
6 S. Xu, Y. Yuan, X. Cai, C.-J. Zhang, F. Hu, J. Liang, G. Zhang, D. Zhang and B. Liu, *Chem. Sci.*, 2015, **6**, 5824–5830.
7 W. Wu, D. Mao, S. Xu, S. Ji, F. Hu, D. Ding, D. Kong and B. Liu, *Mater. Horiz.*, 2017, **4**, 1110–1114.
8 S. Daqiqeh Rezaei, J. Ho, A. Naderi, M. Tavakkoli Yaraki, T. Wang, Z. Dong, S. Ramakrishna and J. K. W. Yang, *Adv. Opt. Mater.*, 2019, **7**, 1900735.
9 S. D. Rezaei, R. J. Hong Ng, Z. Dong, J. Ho, E. H. H. Koay, S. Ramakrishna and J. K. W. Yang, *ACS Nano*, 2019, **13**, 3580–3588.
10 D. Singh, N. Singh, A. Garg and R. K. Gupta, *Compos. Sci. Technol.*, 2019, **174**, 158–168.
11 M. Misra, N. Singh and R. K. Gupta, *Catal. Sci. Technol.*, 2017, **7**, 570–580.
12 A. Lajevardi, M. Tavakkoli Yaraki, A. Masjedi, A. Nouri and M. Hossaini Sadr, *J. Mol. Liq.*, 2019, **276**, 371–378.
13 M. Mosaviniya, T. Kikhavani, M. Tanzifi, M. Tavakkoli Yaraki, P. Tajbakhsh and A. Lajevardi, *Colloid Interface Sci. Commun.*, 2019, **33**, 100211.
14 A. Nouri, M. Tavakkoli Yaraki, A. Lajevardi, Z. Rezaei, M. Ghorbanpour and M. Tanzifi, *Colloid Interface Sci. Commun.*, 2020, **35**, 100252.
15 H. V. Xu, Y. Zhao and Y. N. Tan, *ACS Appl. Mater. Inter.*, 2019, **11**, 27233–27242.
16 E. Assah, W. Goh, X. T. Zheng, T. X. Lim, J. Li, D. Lane, F. Ghadessy and Y. N. Tan, *Colloids Surf., B*, 2018, **169**, 214–221.
17 J. Song, Y. N. Tan, D. Jańczewski, M. A. Hempenius, J. W. Xu, H. R. Tan and G. J. Vancso, *Nanoscale*, 2017, **9**, 19255–19262.
18 P. Chandra, Y. N. Tan and S. P. Singh, *Next generation point-of-care biomedical sensors technologies for cancer diagnosis*, Springer, 2017.
19 N. Seow, Y. N. Tan, L.-Y. L. Yung and X. Su, *Sci. Rep.*, 2015, **5**, 18293.
20 Y. N. Tan, A. Lai and X. Su, *Sci. Adv. Mater.*, 2014, **6**, 1460–1466.
21 N. Seow, Y. N. Tan and L. Y. L. Yung, *Part. Part. Syst. Charact.*, 2014, **31**, 1260–1268.
22 Y. N. Tan, K. H. Lee and X. Su, *RSC Adv.*, 2013, **3**, 21604–21612.
23 Y. N. Tan, K. H. Lee and X. Su, *Anal. Chem.*, 2011, **83**, 4251–4257.
24 K. M. M. Aung, Y. N. Tan, K. V. Desai and X. Su, *Aust. J. Chem.*, 2011, **64**, 1288–1294.
25 Y. N. Tan, X. Su, Y. Zhu and J. Y. Lee, *ACS Nano*, 2010, **4**, 5101–5110.
26 Y. N. Tan, X. Su, E. T. Liu and J. S. Thomsen, *Anal. Chem.*, 2010, **82**, 2759–2765.
27 S. Dinda, F. L. Yap, V. Suresh, R. K. Gupta, D. Das and S. Krishnamoorthy, *Aust. J. Chem.*, 2013, **66**, 1034–1038.
28 M. Tavakkoli Yaraki, S. Daqiqeh Rezaei and Y. N. Tan, *Phys. Chem. Chem. Phys.*, 2020, **22**, 5673–5687.
29 M. Tavakkoli Yaraki, S. Daqiqeh Rezaei, E. Middha and Y. N. Tan, *Part. Part. Syst. Charact.*, 2020, 2000027, DOI: 10.1002/ppsc.202000027.
30 Y. Fu, J. Zhang and J. R. Lakowicz, *J. Am. Chem. Soc.*, 2010, **132**, 5540–5541.
31 Z. Zhu, P. Yuan, S. Li, M. Garai, M. Hong and Q.-H. Xu, *ACS Appl. Bio Mater.*, 2018, **1**, 118–124.
32 I. G. Theodorou, Z. A. Jawad, Q. Jiang, E. O. Aboagye, A. E. Porter, M. P. Ryan and F. Xie, *Chem. Mater.*, 2017, **29**, 6916–6926.
33 B. Della Ventura, M. Gelzo, E. Battista, A. Alabastri, A. Schirato, G. Castaldo, G. Corso, F. Gentile and R. Velotta, *ACS Appl. Mater. Inter.*, 2019, **11**, 3753–3762.
34 A. K. Tobias and M. Jones, *J. Phys. Chem. C*, 2019, **123**, 1389–1397.

35 S. Pawar, A. Bhattacharya and A. Nag, *ACS Omega*, 2019, **4**, 5983–5990.
36 S. M. Fothergill, C. Joyce and F. Xie, *Nanoscale*, 2018, **10**, 20914–20929.
37 R. Knoblauch and C. D. Geddes, *Nanoscale*, 2019, **11**, 4337–4344.
38 Z. Qu, P. Duan, J. Zhou, Y. Wang and M. Liu, *Nanoscale*, 2018, **10**, 985–991.
39 I. G. Theodorou, Z. A. R. Jawad, H. Qin, E. O. Aboagye, A. E. Porter, M. P. Ryan and F. Xie, *Nanoscale*, 2016, **8**, 12869–12873.
40 I. G. Theodorou, Q. Jiang, L. Malms, X. Xie, R. C. Coombes, E. O. Aboagye, A. E. Porter, M. P. Ryan and F. Xie, *Nanoscale*, 2018, **10**, 15854–15864.
41 T. Chung, Y. Lee, M.-S. Ahn, W. Lee, S.-I. Bae, C. S. H. Hwang and K.-H. Jeong, *Nanoscale*, 2019, **11**, 8651–8664.
42 O. Planas, N. Macia, M. Agut, S. Nonell and B. Heyne, *J. Am. Chem. Soc.*, 2016, **138**, 2762–2768.
43 L. Bekale, S. Barazzouk and S. Hotchandani, *Part. Part. Syst. Charact.*, 2014, **31**, 843–850.
44 Y. Yu, W. D. Lee and Y. N. Tan, *Mater. Sci. Eng., C*, 2020, **109**, 110525.
45 M. B. Rivas Aiello, J. J. Romero, S. G. Bertolotti, M. C. Gonzalez and D. O. Mártire, *J. Phys. Chem. C*, 2016, **120**, 21967–21975.
46 N. Macia, V. Kabanov, M. Côté-Cyr and B. Heyne, *J. Phys. Chem. Lett.*, 2019, **10**, 3654–3660.
47 N. Macia, R. Bresoli-Obach, S. Nonell and B. Heyne, *J. Am. Chem. Soc.*, 2019, **141**, 684–692.
48 S. M. Mooi and B. Heyne, *Photochem. Photobiol.*, 2014, **90**, 85–91.
49 J. Liang, K. Li, G. G. Gurzadyan, X. Lu and B. Liu, *Langmuir*, 2012, **28**, 11302–11309.
50 J. K. Kim and D.-J. Jang, *J. Mater. Chem. C*, 2017, **5**, 6037–6046.
51 P. Pompa, L. Martiradonna, A. Della Torre, F. Della Sala, L. Manna, M. De Vittorio, F. Calabi, R. Cingolani and R. Rinaldi, *Nat. Nanotech.*, 2006, **1**, 126.
52 Y. Zhang, K. Aslan, M. J. Previte and C. D. Geddes, *Proc. Natl. Acad. Sci. U. S. A.*, 2008, **105**, 1798–1802.
53 N. Macia, R. Bresoli-Obach, S. Nonell and B. J. Heyne, *J. Am. Chem. Soc.*, 2019, **141**, 684–692.
54 N. Macia, V. Kabanov, M. Côté-Cyr and B. Heyne, *J. Phys. Chem. Lett.*, 2019, **10**, 3654–3660.
55 X. Ke, D. Wang, C. Chen, A. Yang, Y. Han, L. Ren, D. Li and H. Wang, *Nanoscale Res. Lett.*, 2014, **9**, 666.
56 X. Gu, J. Yao, G. Zhang, C. Zhang, Y. Yan, Y. Zhao and D. Zhang, *Chem.–Asian J.*, 2013, **8**, 2362–2369.
57 F. Hu, S. Xu and B. Liu, *Adv. Mater.*, 2018, **30**, 1801350.
58 S. D. Xu, Y. Y. Yuan, X. L. Cai, C. J. Zhang, F. Hu, J. Liang, G. X. Zhang, D. Q. Zhang and B. Liu, *Chem. Sci.*, 2015, **6**, 5824–5830.
59 W. Wu, D. Mao, F. Hu, S. Xu, C. Chen, C. J. Zhang, X. Cheng, Y. Yuan, D. Ding and D. Kong, *Adv. Mater.*, 2017, **29**, 1700548.
60 R. Hu, E. Lager, A. Aguilar-Aguilar, J. Liu, J. W. Lam, H. H. Sung, I. D. Williams, Y. Zhong, K. S. Wong and E. Pena-Cabrera, *J. Phys. Chem. C*, 2009, **113**, 15845–15853.
61 F. Hu, X. Cai, P. N. Manghnani, W. Wu and B. Liu, *Chem. Sci.*, 2018, **9**, 2756–2761.
62 Y. Cao, R. Zheng, X. Ji, H. Liu, R. Xie and W. Yang, *Langmuir*, 2014, **30**, 3876–3882.
63 S. R. Lewis, S. Datta, M. Gui, E. L. Coker, F. E. Huggins, S. Daunert, L. Bachas and D. Bhattacharyya, *Proc. Natl. Acad. Sci. U. S. A.*, 2011, **108**, 8577–8582.
64 C. Tedeschi, L. Li, H. Möhwald, C. Spitz, D. von Seggern, R. Menzel and S. Kirstein, *J. Am. Chem. Soc.*, 2004, **126**, 3218–3227.
65 C. Jiang, X. Liu, C. Luo, Y. Zhang, L. Shao and F. Shi, *J. Mater. Chem. A*, 2014, **2**, 14048–14053.
66 U. Raghavendra, M. Basanagouda, R. Melavanki and J. Thipperudrappa, *Plasmonics*, 2018, **13**, 315–325.
67 A. Queiroz, A. Mezacasa, D. Graciano, W. Falco, J.-C. M'Peko, F. Guimarães, T. Lawson, I. Colbeck, S. Oliveira and A. Caires, *Spectrochim. Acta, Part A*, 2016, **168**, 73–77.
68 A. Dragan and C. Geddes, *Phys. Chem. Chem. Phys.*, 2011, **13**, 3831–3838.
69 J. Zhang, Y. Fu, M. H. Chowdhury and J. R. Lakowicz, *J. Phys. Chem. C*, 2008, **112**, 18–26.
70 K. Aslan, I. Gryczynski, J. Malicka, E. Matveeva, J. R. Lakowicz and C. D. Geddes, *Curr. Opin. Biotechnol.*, 2005, **16**, 55–62.
71 A. I. Dragan, E. S. Bishop, J. R. Casas-Finet, R. J. Strouse, J. McGivney, M. A. Schenerman and C. D. Geddes, *Plasmonics*, 2012, **7**, 739–744.
72 Y. Zhang, K. Aslan, M. J. Previte and C. D. Geddes, *J. Fluoresc.*, 2007, **17**, 345–349.
73 B. Choi, M. Iwanaga, H. T. Miyazaki, Y. Sugimoto, A. Ohtake and K. Sakoda, *Chem. Commun.*, 2015, **51**, 11470–11473.
74 R. Hu, N. L. Leung and B. Z. Tang, *Chem. Soc. Rev.*, 2014, **43**, 4494–4562.
75 Y. Huang, F. Hu, R. Zhao, G. Zhang, H. Yang and D. Zhang, *Chem. - Eur. J.*, 2014, **20**, 158–164.
76 F. E. Hernández, S. Yu, M. García and A. D. Campiglia, *J. Phys. Chem. B*, 2005, **109**, 9499–9504.
77 K. Munechika, Y. Chen, J. M. Smith and D. S. Ginger, *Chapter4 in Importance of Spectral Overlap: Fluorescence Enhancement by Single Metal Nanoparticles*, ed. K. Munechika, *et al.*, 2010, pp. 91–118.
78 Y. Chen, K. Munechika and D. S. Ginger, *Nano Lett.*, 2007, **7**, 690–696.
79 M. Bregnhøj, S. Rodal-Cedeira, I. Pastoriza-Santos and P. R. Ogilby, *J. Phys. Chem. C*, 2018, **122**, 15625–15634.